Portable hard x-ray source for nondestructive testing and medical imaging

Craig N. Boyer[a)]
Universities Space Research Associates, Washington, D.C. 20024

Glenn E. Holland
Sachs Freeman Associates, Incorporated, Landover, Maryland 20785

John F. Seely
Naval Research Laboratory, Code 7674, Washington D.C. 20375-5352

A portable hard x-ray source has been developed for nondestructive testing, medical imaging, and flash x-ray radiography. The source is powered by a Marx generator that produces a 200 kV, 1.2 kA pulse of 60 ns full width at half maximum. The x-ray tube is composed of a tungsten anode and a mesh cathode. The time dependence of the voltage, current, and x-ray emission were measured and were in good agreement with computer simulations. The simulation model accounted for the 15 capacitors and 15 spark gap switches of the Marx generator and the perveance of the electron flow across the anode–cathode gap. The simulations indicated that the 5 J energy that was stored in the Marx generator was efficiently delivered to the x-ray tube. The measured x-ray exposure, 34 mR at a distance of 30 cm, was in good agreement with the calculated exposure. X-ray images are presented that demonstrate the capabilities of the x-ray source for medical imaging, nondestructive testing, and flash x-ray radiography. [S0034-6748(98)04906-5]

I. INTRODUCTION

Flash x-ray sources have been developed that are based on cable transformers,[1] Blumlein technology,[2,3] and Marx generators.[4] The motivation for much of this work is to perform nondestructive studies of transient phenomena associated with high-speed motors, pumps, and ballistics. In addition, flash x-ray radiography techniques may be used for dynamical studies of medical and biological systems.

In this article, we describe a pulsed x-ray source that is driven by a Marx generator. The operating characteristics of the x-ray source have been experimentally measured and compared to detailed computer simulations. Based on the simulations, the operating characteristics can be optimized for nondestructive testing and medical applications.

The current pulse delivered to the x-ray tube begins to rise almost simultaneously with the tube voltage and is not delayed as is the case with cable-driven and high-inductance transformer generators. By closely matching the x-ray tube to the Marx generator, the current oscillations at the end of the pulse are minimal. This implies that most of the energy stored in the capacitors is used to accelerate electrons across the anode–cathode gap of the x-ray tube with only a small fraction of the stored energy dissipated by the spark gap switches. The tube impedance at peak current closely matches the surge impedance of the Marx generator, which is the condition for maximum power transfer between the Marx generator and the x-ray tube. The result is an x-ray pulse that is useful for x-ray radiography and that is produced under optimal conditions with a minimal heat load on the anode.

Dissipation of the heat load by cooling and rotation of the anode is not necessary.

II. MARX GENERATOR AND X-RAY TUBE

The Marx generator and the x-ray tube are shown in Fig. 1. The unit is 22 in. long, weighs 26 lb, and is powered by a rechargeable battery. The Marx generator electronics are described in detail in Ref. 5. The Marx generator, in its present configuration, is composed of 15 energy storage capacitors and 15 spark gap switches that are housed in an acrylic pressure vessel that is covered by a coaxial aluminum return-current cylinder. This compact design functions as a fast pulse forming line with low interstage inductance between the energy storage capacitors. The design can conveniently be scaled to higher energy by adding additional capacitors.

The x-ray tube consists of a small vacuum chamber that houses the anode and cathode.[5] The electrical connection to the Marx generator is by means of a commercial ceramic 30 kV feedthrough. The anode is composed of Elkanite (75% tungsten and 25% copper) machined to a conical shape. The cathode is three layers of fine stainless steel mesh in proximity to the sides of the anode cone. The x-ray flux exits the tube through a 0.2 mm thick aluminum vacuum window.

The equivalent circuits for the Marx generator and the x-ray tube are shown in Fig. 2. Indicated are the trigger circuit (stage 1), 14 identical circuits that contain an energy storage capacitor and a spark gap switch (stages 2–15), and the x-ray tube circuit (stage 16). Each energy storage capacitor (C_1–C_{15}) has an associated inductance (L_1 or L_C) and a stray capacitance C_S to ground. Each spark gap switch has an inductance L_g and a resistance R_g. The x-ray tube is modeled by the inductance L_p and the resistance R_p that are

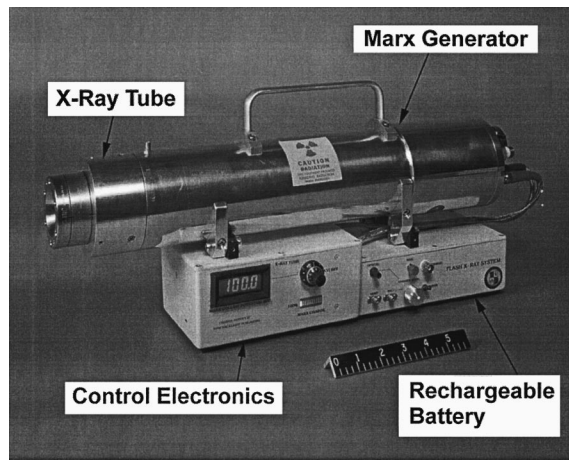[a)]Electronic mail: boyer@uap.nrl.navy.mil

FIG. 1. The Marx generator, x-ray tube, control electronics, and recharge-able battery.

associated with the peaking gap, and by the inductance L_d and voltage V_d associated with the anode–cathode gap.

The x-ray tube current i_{16} was measured by means of a return-current shunt that had a rise time of 1.7 ns.[5] The anode voltage V_d was measured by a capacitive probe with a rise time of 3 ns. The voltage probe was calibrated by a precision resistive shunt. The time dependence of the x-ray pulse was measured by a filtered x-ray photodiode with a rise time of 0.3 ns. The signals were recorded by a digital oscilloscope with 1 GHz bandwidth.

Presented in Fig. 3 are the measured data for 13 consecutive discharges. Each energy storage capacitor was charged to 11 kV. The measured tube current and voltage are shown in Figs. 3(a) and 3(b), and the average peak values are 1.2 kA and 225 kV, respectively. The variation in the peak voltage values was ±2%. The x-ray signal (in arbitrary units) is shown in Fig. 3(c), and the variation was ±8%. The product of the current and voltage, which is a representation of the power delivered to the tube, is shown in Fig. 3(d), and the average peak value was 140 MW with a variation of ±6%. The ratio of the voltage and current (impedance) is shown in Fig. 3(e) and indicates an exponential decay.

The perveance ($i_{16}/V_d^{3/2}$) of the electron flow across the anode–cathode gap is shown in Fig. 3(f) and will be discussed in Sec. III. The electron charge transported across the anode–cathode gap as a function of voltage is related to the x-ray energy distribution and intensity. The charge as a function of voltage is shown in Fig. 3(h) and also will be discussed in Sec. III.

The spike that appears on the rising edge of the measured current pulse, seen in Fig. 3(a), is well simulated by
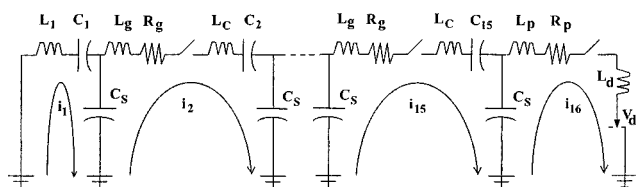

FIG. 2. Equivalent circuits for the trigger (stage 1), the Marx generator (stages 2–15), and the x-ray tube (stage 16).
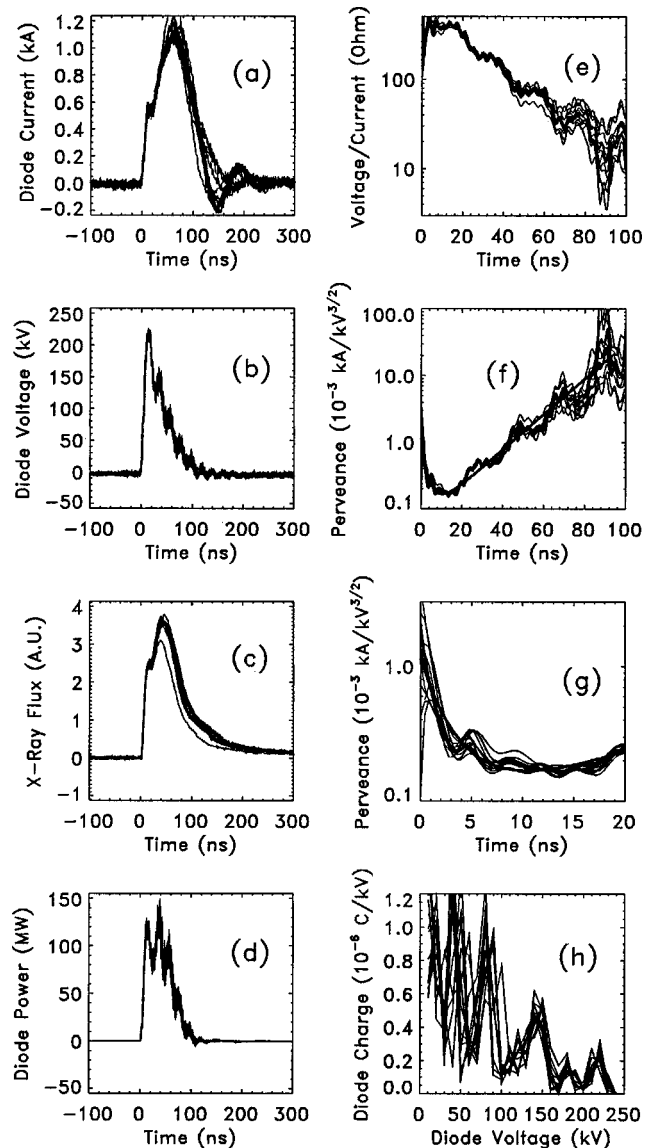

FIG. 3. The measured data for 13 discharges of the x-ray source. (a) Diode current, (b) voltage, (c) x-ray flux, (d) power, (e) impedance, (f) and (g) perveance, and (h) charge.

the computer model that is discussed in Sec. III. This current spike, which occurs at the time of peak voltage, results in a spike on the leading edge of the x-ray pulse as can be seen in Fig. 3(c). The small-amplitude, damped oscillations in the current at times later than 150 ns represent residual ringing of the circuit and are also well simulated.

The 50 MHz oscillation in the measured voltage pulse, seen in Fig. 3(b), is believed to result from a resonance between the lumped inductance of the Marx generator and the stray capacitance between the generator and the wall of the coaxial return current cylinder. These oscillations also appear in the power, impedance, perveance, and charge curves that were derived from the voltage curve.

The measured data indicate an initial electron acceleration phase characterized by high tube perveance with a rapid increase in the tube current and voltage. This is followed by an arc phase in which the current continues to increase while

the voltage and impedance across the tube rapidly collapse in the ensuring vacuum arc. The x-ray energy is relatively high early in the pulse (when the electron acceleration voltage is high) and decreases later in the pulse.

The current, voltage, and x-ray characteristics of the tube were dependent on the anode–cathode separation distance. The data shown in Fig. 3 were recorded using a 4 mm separation. For smaller separation, large tube currents occurred early in the pulse, and the voltage remained low resulting in a large flux of soft x rays. With anode–cathode separation greater than 4 mm, the x-ray pulse was greatly reduced in amplitude and width and was very hard. This suggested that, for a wider separation, the anode–cathode gap remained in the high impedance state longer, and the voltage could therefore continue to increase resulting in harder x rays.

III. COMPUTER SIMULATIONS

The computer simulations were based on the equivalent circuit shown in Fig. 2. An equation was written for each of the 16 stages:

$$(1/C_1 + 1/C_s)q_1 + L_1(di_1/dt)$$
$$= q_2/C_s - (dC_1/dt)(V_0 - q_1/C_1),$$

where

$$q = \int_0^t i\,dt,$$

$$(1/C_n + 2/C_s)q_n + (L_g + L_c)(di_n/dt) + R_g i_n$$
$$= V_0 + (q_{n-1} + q_{n+1})/C_s - (dC_n/dt)(V_0 - q_n/C_n)$$

where $n = 2-15$, and

$$q_{16}/C_s + (L_p + L_d)(di_{16}/dt) + R_p i_{16} = V_0 - V_d + q_{15}/C_s.$$

The first equation represents the trigger circuit, the second equation the 14 identical stages containing energy storage capacitors, and the last equation the x-ray tube. These 16 time-dependent equations were solved for the currents by a fourth-order Runge–Kutta algorithm.

The various inductances that appear in the equations were calculated *ab initio* and had fixed values. The inductances were $L_1 = 24.15$, $L_g = 22.14$, $L_C = 1.37$, $L_p = 10.24$, and $L_d = 50$ nH.

The capacitance of the energy storage capacitors was 8.325 nF for the case of no applied voltage. However the capacitance of barium titinate capacitier is voltage dependent and decreases with applied voltage. For example, the capacitance is reduced by 33% for a charging voltage of 11 kV. The capacitance was modeled by the expression $C_n = C_0(1 - k)$ where $C_0 = 8.325$ nF and k increased with applied voltage as indicated by the manufacturer. The stray capacitance was calculated to be $C_s = 2.15$ pF.

The effective resistance of the spark gap switches was a free parameter in the calculation. The resistance was determined by matching the calculated ringing of the current late in the pulse to the measured data. The 15 resistance values (R_g and R_p) were set equal to 0.8 Ω. Thus the total resistance in the Marx generator and the x-ray tube was 12 Ω.
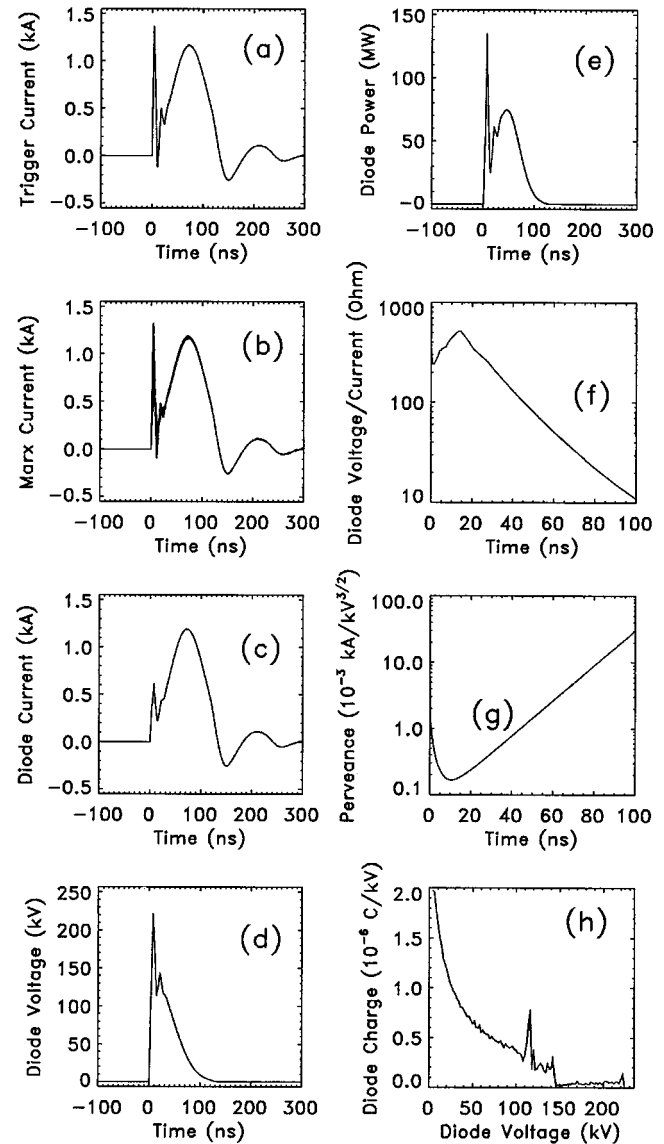

FIG. 4. The results that were calculated using the equivalent circuits for the Marx generator and the x-ray tube. (a) Trigger current, (b) Marx current, (c) diode current, (d) diode voltage, (e) diode power, (f) diode impedance, (g) perveance, and (h) charge.

In the simulation model, the current and voltage across the anode–cathode gap were related by the Langmuir–Child law $i_{16} = PV_d^{3/2}$ where P is the perveance of the electron flow. An attempt was made to use an analytical expression for the perveance that had a simple dependence on time and on the anode–cathode separation and width.[6] However, it was found that even the simple expressions that were previously derived in an attempt to understand the explosive emission of electrons[7] did not accurately model the perveance of the x-ray tube. We therefore used in the simulation model a semiempirical perveance that was derived from the measured current and voltage. Using the least squares technique, an analytical curve was fitted to the measured values of $i_{16}/V_d^{3/2}$ for the 13 discharges. The fitted curve is the smooth curve shown in Figs. 3(f) and 3(g) and also in Fig. 4(g). The initial exponential decrease in the perveance early in the pulse and the exponential increase late in the pulse are essential for the accurate modeling of the x-ray tube. The accurate determi-
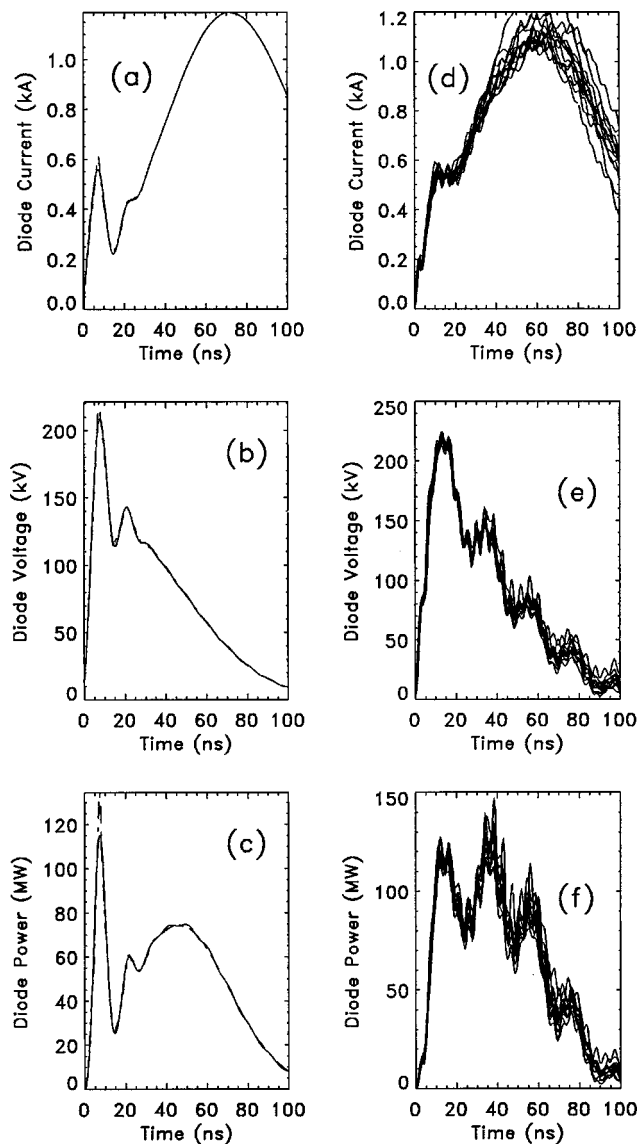
FIG. 5. Comparison of (a)–(c) the calculated quantities and (d)–(f) the measured quantities during the early part of the pulse. (a) and (d) Diode current, (b) and (e) diode voltage, and (c) and (f) diode power.

nation of the perveance was made possible by the measurement of the rapidly changing current and voltage at the leading edge of the pulse.

The results of the simulation are shown in Figs. 4–7. Figures 4(a)–4(h) show the calculated trigger current i_1, currents $i_2 - i_{15}$, x-ray tube current i_{16}, tube voltage V_d, tube power $i_{16} V_d$, tube impedance V_d / i_{16}, perveance $i_{16}/V_d^{3/2}$, and tube charge (the total charge was 0.1 mAs), respectively. These may be compared to the corresponding measured quantities shown in Fig. 3.

More detailed comparisons of the measured and the calculated tube current, voltage, and power at the beginning of the pulse are shown in Fig. 5. In Figs. 5(a)–5(c), the dashed curves (which are barely visible) are the calculated values, and the solid curves are the calculated values filtered by a 200 MHz low pass filter. The low pass filter was included in the calculation to simulate the effect of the attenuation filters that were used to protect the oscilloscope from large input voltages. It is apparent that the oscillations in the measured

voltage (and in the other quantities that were derived from the measured voltage) do not result from the attenuation filters. As previously mentioned, these oscillations are believed to result from a resonance between the lumped inductance of the Marx generator and the stray capacitance between the generator and the wall of the coaxial return current cylinder.

We note that the only free parameter in the simulation model was the resistance of the spark gap switches. This resistance was established by matching the frequency of the small-amplitude ringing of the tube current to the measured frequency. The inferred resistance was 0.8 Ω for each spark gap switch. By varying the spark gap resistance about this value, it was found that the assumed spark gap resistance had little effect on the calculated current and voltage early in the pulse. Thus the good agreement between the calculated and measured current and voltage shown in Fig. 5 did not depend on the assumed resistance. In effect, there were no free parameters in the calculation of the current and voltage early in the pulse, and the agreement between the calculations and measurements is remarkably good. Stated another way, the good agreement between the calculated and measured current and voltage indicates that the semiempirical perveance is an accurate representation of the electron flow across the anode–cathode gap and that the circuit parameters (capacitances and inductances) that were calculated in an *ab initio* manner are also accurate.

The time-dependent energy balance was calculated by accounting for the energies of each of the electronic components in the equivalent circuits (Fig. 2). In Fig. 6(a), the curves labeled C_C and C_S indicate the energies associated with the storage capacitance and the stray capacitance, respectively. In Fig. 6(b), the curves labeled L_C, L_G, and L_T indicate the energies associated with the inductances of the storage capacitors, the spark gap switches, and the x-ray tube. In Fig. 6(c), E_R is the energy dissipated by the various resistances, and E_D is the energy term $\int (V_0 - q/C) dC$ associated with the change in the capacitance of the storage capacitors with applied voltage.

In Fig. 6(d), the sum of the energies associated with all capacitances, inductances, and resistances is indicated by E_C, E_L, and E_R. E_T indicates the energy delivered to the anode–cathode gap $\int i_{16} V_d dt$. E_{TOT} indicates the sum of all of the energy terms. This total energy is not exactly constant with time, and this may result from a somewhat incomplete representation of the equivalent circuits of the Marx generator and the x-ray tube.

It is apparent from the curves labeled E_C and E_T in Fig. 6(d) that practically all of the 5 J of energy that is initially in the energy storage capacitors is delivered to the anode–cathode gap of the x-ray tube. This results from the excellent matching of the impedance of the Marx generator to the x-ray tube.

The energy delivered to the anode–cathode gap, as a function of the electron acceleration voltage, was calculated from the time-dependent current and voltage and is shown in Fig. 6(e). The energy delivered at the higher voltages (>150 kV) occurs primarily during the time of the spike on the leading edge of the current pulse when the voltage is maximal (see Fig. 5). The energy delivered at voltages of
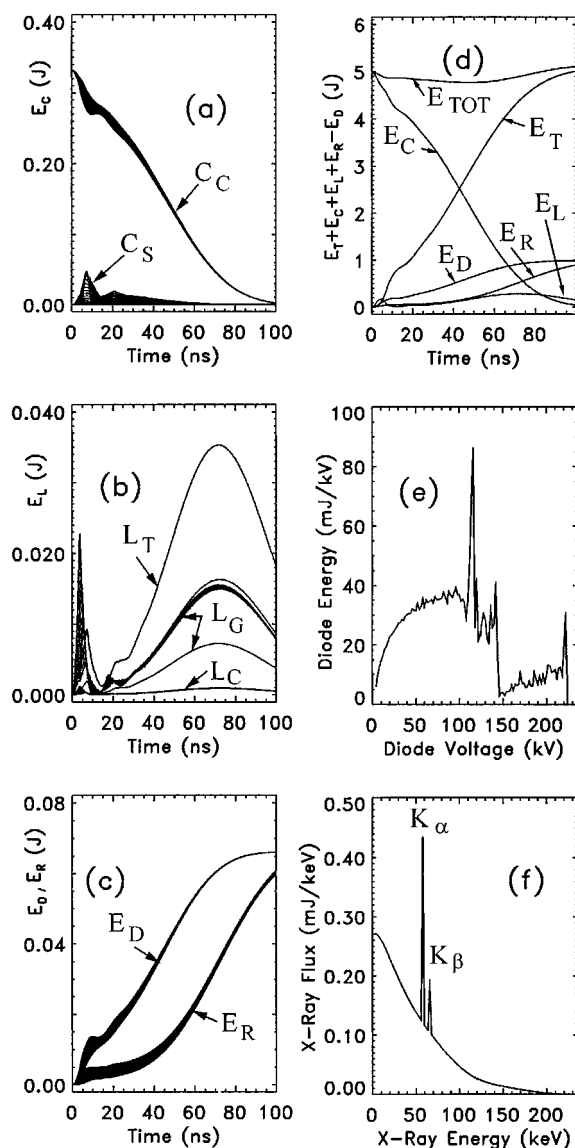
FIG. 6. (a)–(d) The calculated energies, (e) the energy deposited in the anode–cathode gap, and (f) the x-ray flux.
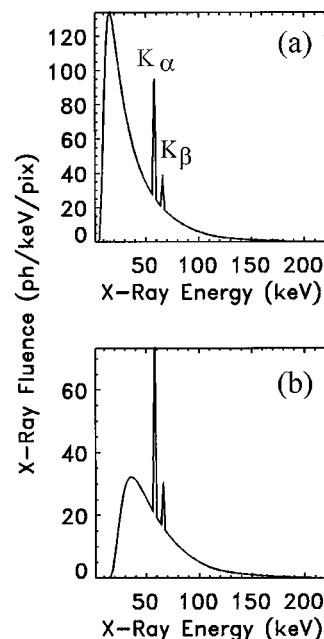

FIG. 7. (a) The calculated x-ray fluence at a distance of 30 cm from the source and (b) the x-ray fluence with an additional attenuation by 3 mm of aluminum.

50–150 kV occurs primarily during the middle of the current pulse when the current is high and the voltage is decreasing. This illustrates the dual energy nature of the x-ray source, with harder x rays emitted early in the discharge and softer x rays in the following arc stage of the discharge.

The x-ray spectrum was calculated from the current and voltage using a thick-target bremsstrahlung model and accounting for the tungsten K_α and K_β radiation.[8–10] The x-ray spectrum, in units of mJ per keV of x-ray energy, is shown in Fig. 6(f). The energy in the characteristic K_α and K_β x-ray lines is 0.8 mJ, and the energy in the continuum is 16 mJ. The efficiency of conversion of the electrical energy to x-ray energy is 0.34%.

IV. X-RAY FLUX AND IMAGES

In order to determine the utility of the x-ray source for single-discharge radiography, the x-ray fluence was calculated at a distance of 30 cm from the x-ray source. It was assumed that the size of the detector resolution element was

48 μm. This is the pixel size of an x-ray charge coupled device (CCD) sensor that was used to record some of the images. The calculation accounted for the attenuation by the 0.2 mm thick aluminum window in the x-ray tube. The x-ray fluence, in units of photons per pixel per keV of x-ray energy, is shown in Fig. 7(a). The number of x rays incident per pixel is sufficiently large to be detected up to an x-ray energy of approximately 150 keV.

The x-ray exposure was determined by calculating the energy-dependent ionization of air using the technique of Ref. 11. The total exposure, summed over x-ray energy, was 41 mR (where 1 mR is equivalent to an ionization charge of 2.58×10^{-4} C per 1 g of dry air). This may be compared to the single-discharge exposure of 34 mR that was measured by a pocket dosimeter at a distance of 30 cm from the x-ray source.

The x-ray fluence with an additional attenuation by 3 mm of aluminum is shown in Fig. 7(b). In this case, the exposure is 4 mR. The entrance skin dose was estimated by using the energy-dependent attenuation coefficient of water, and the calculated dose was 8 mrad (where 1 mrad represents an absorbed energy of 0.1 erg per 1 g of absorbing material).

The x-ray emission from the anode was imaged with a pinhole camera consisting of a 0.5 mm hole drilled through a 2 mm lead sheet. The x-ray image was converted to 584 nm light by a 50 μm thick terbium-doped Gd_2O_2S scintillator. The scintillator was pressed against the face of a CCD imaging sensor with 760×524 pixel format and 48 μm pixel spacing. The detector package was covered with 1.5 mm thick aluminum sheet to harden the x-ray flux and to exclude visible light. After accounting for the magnification factor of the pinhole camera, the size of the x-ray emission region was determined to be 3 mm.
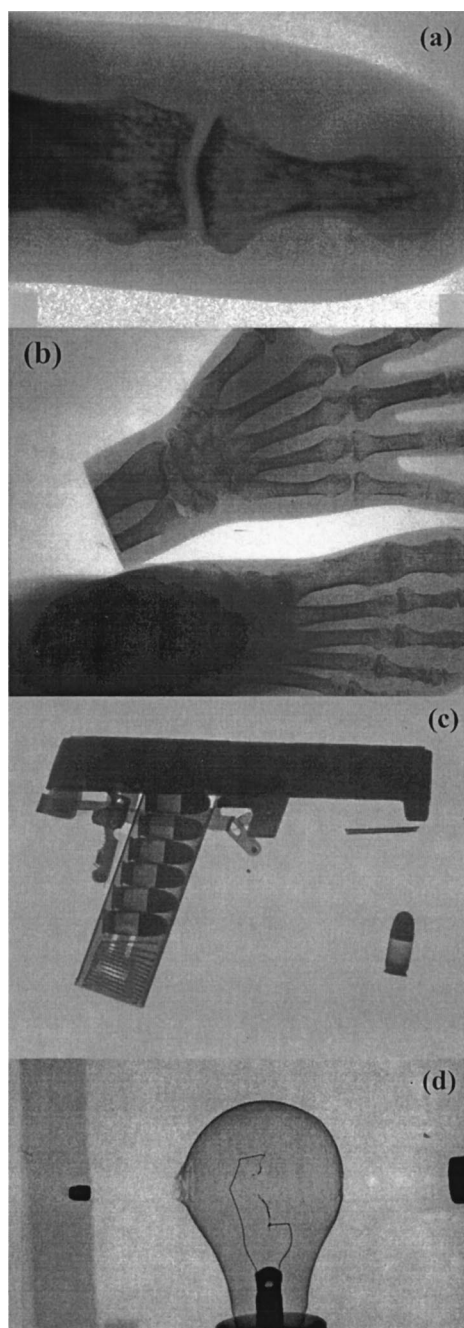
FIG. 8. The x-ray images of (a) a finger of a hand phantom, (b) hand and foot phantoms, (c) the revolver, and (d) the bullet that is entering a wooden board after passing through a light bulb.

Using a lead step wedge, it was found that x-ray energies as high as 150 keV could be detected. Since the fluence at higher energies may have been too weak to detect, these results are consistent with the calculated x-ray fluence.

Shown in Fig. 8 are typical x-ray images recorded by a single discharge of the x-ray source. The image of a finger of a hand phantom is shown in Fig. 8(a). The image was recorded by the CCD sensor. The distal phalangeal tuft, distal interphalangeal joint, and tesselations in the joint region are clearly visible.

Figure 8(b) is the image of a hand phantom and a foot phantom that was recorded using a Rarex green screen and Polaroid 803 large-format film. This illustrates the size and uniformity of the exposure field. Figure 8(c) is the image of a revolver and illustrates the capability of the x-ray source for nondestructive examination and surveillance.

Shown in Fig. 8(d) is the flash x-ray image of a rifle bullet that has passed through a light bulb and severed the filament. The muzzle of the rifle is visible at the right side of the image. At the time this image was recorded, the bullet had just entered a wooden board at the left side of the image, and the tip of the bullet is slightly flattened (the bullet continued to pass through the board). The x-ray source was triggered by the flash of visible light from the muzzle. A precision delay generator was used to delay the x-ray discharge with respect to the muzzle flash. It was found that the x-ray source could be triggered reproducibly so that the bullet could be viewed at various distances from the muzzle, including inside the bulb. We note the ring features that are concentric about the exit hole in the bulb. These are probably shock waves propagating from the exit hole. This image illustrates the ability to reliably trigger the x-ray source for the purpose of recording flash images of transient phenomena.

V. DISCUSSION

A variety of x-ray images were recorded using a single discharge of the x-ray source. The images illustrated the capabilities of the x-ray source for medical radiography, nondestructive testing and examination, surveillance, and flash radiography of transient phenomena. Since the x-ray source is battery powered, compact, and lightweight, it may be used in confined spaces and in remote locations where electrical power is not available.

An interesting feature of the simulations and the data shown in Fig. 5 is that the current pulse begins to rise almost simultaneously with the tube voltage and is not delayed as is the case with cable-driven and high-inductance transformer generators. By closely matching the x-ray tube to the Marx generator, the current oscillations at the end of the pulse (after the anode–cathode gap has shorted) are minimal. This implies that most of the energy stored in the capacitors is used to accelerate electrons across the anode–cathode gap of the x-ray tube with only a small fraction of the stored energy dissipated by the spark gap switches. This is confirmed by the energy balance calculations shown in Fig. 6(d).

The spike on the leading edge of the current pulse, as seen in both the simulations and data shown in Fig. 5, occurs at the time of greatest accelerating potential across the anode–cathode gap and therefore results in a spike in the x-ray pulse [Fig. 3(c)]. After the current spike, the x-ray flux continues to increase with current while the energy of the emitted x rays decreases. The tube impedance at peak current closely matches the surge impedance of the Marx generator, which is the condition for maximum power transfer between the Marx generator and the x-ray tube. The result is an x-ray pulse that is useful for x-ray radiography and one that is produced under optimal conditions with a minimal heat load on the anode.

[1] A. Khacef, R. Viladrosa, C. Cachoncinlle, E. Robert, and J. M. Pouvesle, Rev. Sci. Instrum. **68**, 2292 (1997).

[2] Q. Johnson, A. C. Mitchell, and I. A. Smith, Rev. Sci. Instrum. **51**, 741 (1980).

[3] C. B. Collins, R. Davanloo, and T. S. Brown, Rev. Sci. Instrum. **57**, 863 (1986).

[4] M. N. Kekez, Rev. Sci. Instrum. **62**, 2923 (1991).

[5] C. N. Boyer, G. E. Holland, and J. F. Seely, Coherent Electron-Beam X-Ray Sources, edited by A. K. Freund, H. P. Freund, and M. R. Howells, SPIE Proceedings Vol. 3154 (1998), p. 16.

[6] G. A. Mesyats, Sov. Phys. Tech. Phys. **19**, 948 (1975).

[7] S. P. Bugaev, E. A. Litvinov, G. A. Mesyats, and D. I. Proskurovskii, Sov. Phys. Usp. **18**, 51 (1975).

[8] M. Green and V. E. Cosslett, Proc. Phys. Soc. London **78**, 1206 (1961).

[9] P. Tothill, Br. J. Appl. Phys., J. Phys. D **1**, 1093 (1968).

[10] R. Birch and M. Marshall, Phys. Med. Biol. **24**, 505 (1979).

[11] J. D. Cox, D. W. Williams, and D. S. Langford, Physics of Medical Imaging, edited by R. Shaw, SPIE Proceedings Vol. 2163 (1994), p. 284.